PROCEEDINGS PAPER

Characterization of MoS_2 films via simultaneous grazing incidence X-ray diffraction and grazing incidence X-ray fluorescence (GIXRD/GIXRF)

Mark A. Rodriguez [a], Tomas F. Babuska, John Curry, James J. M. Griego, Mike T. Dugger, Steven R. Larson, and Alex Mings
Sandia National Laboratories, Albuquerque, NM 87185-1411, USA

(Received 29 March 2024; accepted 3 April 2024)

Physical vapor deposited (PVD) molybdenum disulfide (nominal composition MoS_2) is employed as a thin film solid lubricant for extreme environments where liquid lubricants are not viable. The tribological properties of MoS_2 are highly dependent on morphological attributes such as film thickness, orientation, crystallinity, film density, and stoichiometry. These structural characteristics are controlled by tuning the PVD process parameters, yet undesirable alterations in the structure often occur due to process variations between deposition runs. Nondestructive film diagnostics can enable improved yield and serve as a means of tuning a deposition process, thus enabling quality control and materials exploration. Grazing incidence X-ray diffraction (GIXRD) for MoS_2 film characterization provides valuable information about film density and grain orientation (texture). However, the determination of film stoichiometry can only be indirectly inferred via GIXRD. The combination of density and microstructure via GIXRD with chemical composition via grazing incidence X-ray fluorescence (GIXRF) enables the isolation and decoupling of film density, composition, and microstructure and their ultimate impact on film layer thickness, thereby improving coating thickness predictions via X-ray fluorescence. We have augmented an existing GIXRD instrument with an additional X-ray detector for the simultaneous measurement of energy-dispersive X-ray fluorescence spectra during the GIXRD analysis. This combined GIXRD/GIXRF analysis has proven synergetic for correlating chemical composition to the structural aspects of MoS_2 films provided by GIXRD. We present the usefulness of the combined diagnostic technique via exemplar MoS_2 film samples and provide a discussion regarding data extraction techniques of grazing angle series measurements.

[doi:10.1017/S0885715624000319]

Key words: grazing incidence X-ray diffraction, grazing incidence X-ray fluorescence, solid lubricant, MoS_2

I. INTRODUCTION

Molybdenum disulfide (MoS_2) films are employed as solid lubricant materials for applications in aerospace (Gao et al., 2017; Babuska et al., 2022b). Many of these applications involve coating steel parts to reduce friction and wear at mechanical interfaces including latches, deployment mechanisms, and gears (Hilton and Fleischauer, 1992; Macknojia et al., 2023). The important morphological characteristics of MoS_2 films include density, thickness, stoichiometry, observed phase, and crystallographic orientation, all of which play a crucial role in determining wear rate, initial coefficient of friction, and resistance to oxidation from environmental species such as water (termed aging) and atomic oxygen (Khare and Burris, 2014; Curry et al., 2016, 2017; Gao et al., 2017; Lince et al., 2019; Chrostowski et al., 2023). These microstructural characteristics cannot easily be determined by a single characterization method and can require expensive and time-consuming methods such as Rutherford backscattering spectroscopy (RBS) or transmission electron microscopy (TEM), techniques that are challenging to use for quality control and process development (Babuska et al., 2022a). Ideally, to optimize the tribological performance of a film, one would need a comprehensive, nondestructive characterization method that enables access to all the above-mentioned film characteristics to provide insight into structure–property–performance relationships. X-ray diffraction (XRD) can be employed for diagnosis of the phase identification and crystallographic orientation, but composition can only be inferred indirectly via phase identification. In contrast, standard X-ray fluorescence (XRF) methods can be employed to estimate thickness via X-ray beam attenuation, as well as composition via emission line intensities. However, XRF suffers drawbacks as well. For example, XRF will struggle to distinguish between a thin high-density film and a thick low-density film. This is a particularly challenging issue if film thickness is employed as a sole requirement for

[a]Author to whom correspondence should be addressed. Electronic mail: marodri@sandia.gov

acceptance, and considerable risks are inherent in such a singular approach. For instance, a thin high-density coating is desirable because aging resistance is increased, but if the film is too thin, then coverage of complex geometries may be insufficienct, resulting in high friction regions. On the other hand, a low-density coating may be determined to be of sufficient thickness yet is susceptible to oxidation, causing premature failure of the coating and potential component seizure (Babuska et al., 2023). This indistinguishable variation is compounded by the fact that XRF reveals little about the microstructure and grain orientation. The complimentary nature of XRD and XRF serve well to enable a clearer picture by providing the information missing from each individual method. In addition, the use of grazing incidence geometry for data collection enhances signal from a thin MoS_2 film (<1 μm) when deposited on bulk metallic substrates. We present results for the simultaneous collection of both grazing incidence X-ray diffraction (GIXRD) and grazing incidence X-ray fluorescence (GIXRF) to evaluate MoS_2 film morphologies deposited via physical vapor deposition (PVD) across varying processing conditions. The analysis will serve to isolate film characteristics such as density and composition from that of film thickness, and establish a robust means of film diagnostic measurement that nondestructively evaluates the film in these four critical characteristics: density, microstructure (texture), composition, and thickness. A more comprehensive diagnosis of the deposited film can thereby improve prediction of its ultimate performance and support acceptance criteria by establishing quality control metrics and allowing for rapid process development.

II. EXPERIMENTAL

A. Film synthesis

Stainless steel (13-8 PH, mirror polished $R_a < 20$ nm) coupons were cleaned via isopropyl sonication and loaded into a custom-built sputtering deposition system. An additional silicon witness substrate (partially masked with tape to create a step in the deposited film) was also loaded for the determination of deposited film thickness. The chamber was pumped down to a base pressure of $<1 \times 10^{-6}$ Torr. An initial Ti (99.995% Kurt J. Lesker) adhesion layer (100 nm thickness) was deposited via DC sputtering at 3 mTorr and 150 W. Next, the MoS_2 (99.9% Kurt J. Lesker) material was deposited using the various conditions including Argon chamber pressure (3 mTorr vs. 10 mTorr), wattage (100 W vs. 200 W), and the presence of a substrate bias (−100 VSB), as outlined in Table I. The resulting MoS_2 films demonstrated widely varying properties and characteristics. The deposited thicknesses were verified by profilometry on the witness samples using a Bruker DektakXT stylus profilometer.

Density and S:Mo atomic ratio were derived by RBS measurements and serve as ground truth (i.e., real values) for the films prior to X-ray scattering. Because RBS is a costly analysis requiring a high-energy ion beam line, the primary motivation of our work was to establish an inexpensive, nondestructive means for enabling film diagnostics without the need for routine RBS analysis. In like manner, ground truth (real) film thickness was determined via profilometer step height measurements. This measurement was performed on the silicon witness coupon and could not be performed on engineered parts without masking. It is desired that XRF analysis be correlated to the profilometer measured thicknesses in order to calibrate the nondestructive XRF method for film coating thickness determination beyond that of witness coupons. Table I also reports nanoindentation hardness (Hysitron TI 980 TriboIndenter) and wear rate (see Bassett et al., 2023) for several of the films that have sufficient thickness such as to not influence the reported measurement. This set of nine films with differing characteristics and properties served as a good test matrix for our X-ray diagnostic methodology. Table I is employed throughout the article to give context to the observed GIXRD and GIXRF results. This article will focus mostly on three films: M163, M167, and M170. Each of these films share a similar thickness value (~470 to 490 nm) and serve as exemplars for their different deposition conditions. Film M163 would be considered a "good" film with acceptable properties, while film M167 would be considered a "bad" film with unacceptable properties. Film 170 is an interesting film with a substantially lower S:Mo ratio and is added for comparison purposes to round out the various observed film microstructures in the test matrix. In this article, the deposited films will be discussed generically as MoS_2 films with an awareness that the S:Mo ratio varies significantly depending on deposition conditions as shown in Table I.

B. Instrumentation

GIXRD measurements were performed using a Siemens D500 $\theta-2\theta$ X-ray diffractometer configured for grazing incidence. Figure 1 shows the configuration of the instrument.

The diffractometer was equipped with a sealed tube X-ray anode (Cu Kα/40 kV, 30 mA), parallel-beam optic soller attachment, LiF monochromator, and scintillation detector. A series of grazing incidence angles (0.2°–2.0° in 0.1° steps) was measured for all film samples. Additionally, an Amptek X-123 silicon drift detector (SDD) was positioned at ~130° 2θ and the beam path to this XRF detector was

TABLE I. Deposition conditions and resulting film characteristics and properties.

Film name	Deposition process	Thickness (nm)	Density (g cm^{-3})	S:Mo ratio via RBS	Hardness (GPa)	Wear rate (10^{-7}mm^3/N*m)
M163	100 W DC 3mTorr Ar	**475**	5.02	1.63	5.5	4.6
M164		232	5.04	1.63		
M165		58	4.28	1.63		
M167	200 W RF 10 mTorr Ar	**488**	2.16	1.96	0.62	160–16.2
M168		162	3.08	1.78		
M169		48	2.93	1.65		
M170	200 W RF 3 mTorr Ar–100 VSB	**472**	4.83	0.93	9.26	
M171		212	5.50	0.93		
M172		75	6.10	0.93		0.53

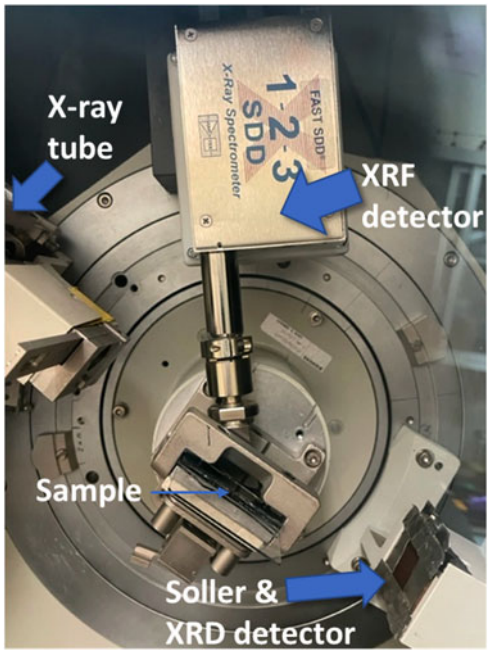

Figure 1. Siemens D500 diffractometer equipped for GIXRD and simultaneous GIXRF via Amptek XRF detector.

controlled via a pinhole collimator with a soller slit attached to the end of the collimator housing. This configuration served to isolate the scattered fluorescence X-rays coming from the sample from other additional X-ray scatter from the instrumentation, thereby reducing noise and spurious signals at the XRF detector during data collection.

Standard XRD analysis was also performed via a Siemens D500 $\theta-\theta$ diffractometer configured with a Cu Kα sealed tube anode source (40 kV, 30 mA), graphite monochromator, and scintillation detector. Measurements were collected overnight to improve signal-to-noise from the films.

III. RESULTS AND DISCUSSION

A. Standard XRD analysis

Figure 2 reveals the standard out-of-plane (symmetric) XRD patterns for films M163, M167, and M170. The samples show strong diffraction peaks for a body-centered cubic (BCC) martensitic steel phase, with small peaks related to the face-centered cubic (FCC) austenitic trace phase. These peaks are attributed to the substrate (13-8 PH stainless steel) and were present in all XRD patterns. All other intensity in the patterns is associated with the MoS_2 film. The films reveal very different diffraction patterns depending on their deposition parameters and overall pedigree. While film M163 shows a pattern consistent with a *c*-axis out-of-plane oriented film as denoted by the strong MoS_2 (002) reflection at ~13.5° 2θ, film M167 shows a pattern devoid of the characteristic (002) peak and instead shows significant intensity for the (100) peak at ~33° 2θ, indicating that the film presents an *a*-axis out-of-plane grain orientation preference.

The ultra-low coefficient of friction ($\mu < 0.05$) behavior of MoS_2 and use as a solid lubricant stems from the layered nature of the structure where molybdenum sulfide atoms form 2D sheets along the *a*–*b* crystallographic plane (Curry et al., 2016). These 2D sheets are held together via weak Van der Walls forces as the sheets stack up to form a lamella-type structure along the *c*-axis direction, thereby enabling a low shear-strength in the direction of mechanical sliding. For film M163, these 2D layers stack such that the sheets lay parallel to the metal substrate (termed basally oriented). It is worth pointing out here that the wear rate of the M163 film is low, i.e., 4.7×10^{-7} mm^3/N*m as shown in Table I. This low wear rate, coupled with a high density of ~5 g cm^{-3} (bulk $MoS_2 = 5.06$ g cm^{-3}) and a high hardness (5.5 GPa), are characteristic of a desired solid lubricant film. In contrast, Table I shows that M167 has wear rates ranging from 16.2 to 160×10^{-7} mm^3/N*m, a factor of at least ~3.5 times that of M163. In addition, the 2.16 g cm^{-3} density of film M167 is ~2× lower than M163 and indicates a significant amount of porosity. Likewise, the hardness of the M167 film is shown to be greatly diminished (0.62 GPa) when compared to the M163 film. The low density and hardness are both structural indicators that trend with the high wear rate of the M167 film. It is worth noting that the S:Mo ratio is highest for the M167 film, at nearly a 2:1 ratio, making it near stoichiometric to the expected MoS_2 formula. However, this did not enable the best performance for wear rate owing to the other aspects of the film (low hardness, density, and crystalline orientation). Films M163 and M167 yield a great deal of insight regarding

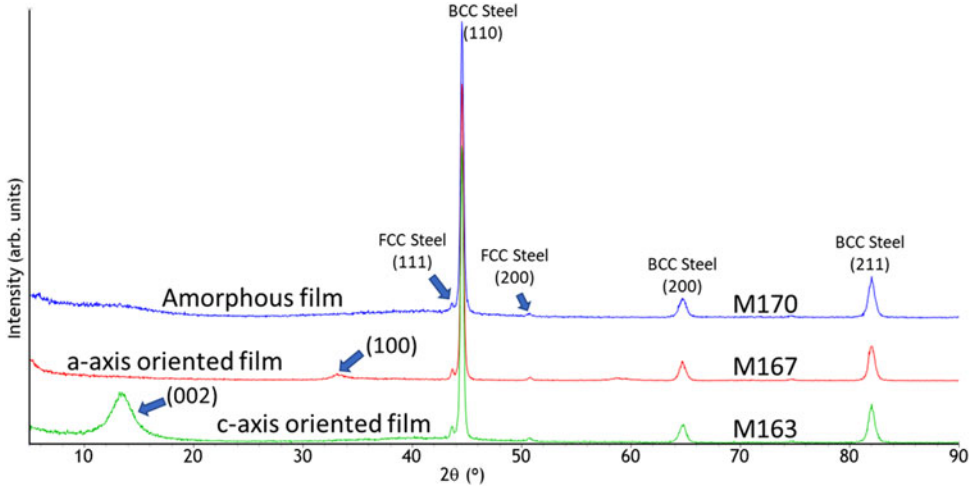

Figure 2. XRD patterns for exemplar films M163 (*c*-axis), M167 (*a*-axis), and M170 (amorphous).

the ideal structural characteristics of deposited MoS_2 films. In addition, it is worth addressing the remaining M170 film, as shown in Figure 2. The standard XRD pattern for film M170 shows an amorphous pattern, with little evidence of intensity in peak locations for either the (002) or (100). Table I shows high density and hardness values of 4.83 g cm^{-3} and 9.26 GPa, respectively. It is clear from the RBS analysis that the S:Mo ratio is quite low for this film series M170, M171, and M172 with a S:Mo ratio of 0.93, making these films substantially Mo-rich with respect to the 2:1 molar ratio of S:Mo. However, even with this low S content, the wear rate performance for this film type was excellent, yielding a value of 0.53×10^{-7} $mm^3/N*m$ value for film M172, the thinnest film coating of that series. Unfortunately, only the M172 film could be tribologically tested. As the films became thicker for M171 and M170, they demonstrated full film failure and delamination due to high film stress resulting from the high voltage bias deposition process. So, while the amorphous films look to possibly excel in wear resistance, they remain impractical due to a lack of film adhesion and ability for high bias deposition conditions to be replicated on parts with complex geometries. Taken together, these three film types: *c*-axis, *a*-axis, and amorphous, serve to yield highly practical details regarding film performance. The key to success for our effort to establish a nondestructive X-ray based analysis stems from the ability to measure composition, density, and crystalline orientation, in addition to film coating thickness. This can be accomplished via the use of GIXRD/GIXRF.

B. GIXRD analysis

Figure 3 shows three stack plots of the GIXRD measurement series for the three exemplar films. First, the M163 film (Figure 3, left) shows the characteristic (002) peak, similar to that of the standard XRD pattern shown in Figure 2. While the patterns in Figure 3 are GIXRD data and therefore asymmetric diffraction conditions, the diffraction peaks at lower 2θ angles more closely resemble that of the symmetric patterns because the in-plane nature of Bragg scattering is reduced at low 2θ. What is of great interest in the stack plot for M163 (Figure 3, left) is that the (002) peak is *absent* at the lowest grazing incidence angles of 0.2° and 0.3°. The (002) peak appears for the 0.4° scan and remains present for the remainder of the series up to 2.0°. The delayed onset of this peak is an indication of a higher density film as will be discussed shortly. In contrast, film M167 (Figure 3, middle) reveals the absence of the (002) peak, but detection of the overlapped (100) and (101) peaks for MoS_2, highlighting the *a*-axis out-of-plane nature of the film (within a range of mosaic spread). It is important to point out that for film M167, the intensity for the (100) and (101) overlapped peaks shows an *earlier onset* of detected intensity, as seen by the easily detected peak in the 0.3° grazing angle pattern. The detection of intensity at lower grazing angles in the grazing angle series is indicative of a low-density film. Finally, for the M170 film, Figure 3 (right), we observe similar delayed intensity onset for the stack plot series. While it is difficult to detect the onset of scattering intensity for an amorphous film, the deviation of the pattern profile for the 0.4° grazing angle pattern specifically at ~40° 2θ is noted relative to the nearly flat background level for the 0.2° and 0.3° patterns in this same 2θ location. Therefore, the M170 film also indicates the presence of a dense film similar to that of M163.

To confirm the correlation between density and delayed onset of film scattered intensity, simulations were performed to determine the beam penetration behavior for Cu Kα X-rays. Figure 4 shows a graph of beam penetration depth vs. grazing angle for the three films. This graph was simulated using the data available from Lawrence Berkeley National Laboratory (Henke et al., 1993) as well as private discussions with Gerhad Martens (Martens, 2023). Note that for film M167, the modeling indicates beam penetration into the film even at a grazing angle of 0.2°, with a pronounced depth of penetration of ~150 nm by 0.3°. In contrast, films M163 and M170 show minimum beam penetration in the range of 0.2°–0.3°, with the onset of significant scattering observed by 0.4°. This effect is similar to X-ray reflectivity (XRR) where higher density films display a shift in the critical edge to higher 2θ angles (Chason and Mayer, 1997). Considering GIXRD scan geometry and the limited penetration depth at low angles, we expect that Bragg scattering from the film

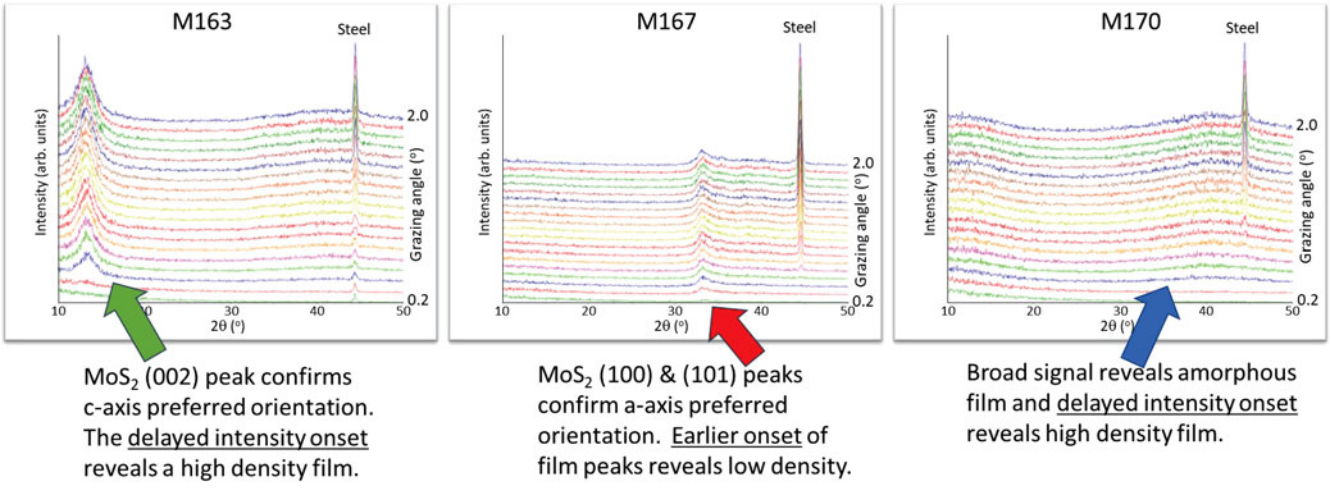

Figure 3. Stacked GIXRD patterns for film M163 (left), M167 (middle), and M170 (right). Detection of delayed onset of scattering to higher grazing angles reveals a higher film density.

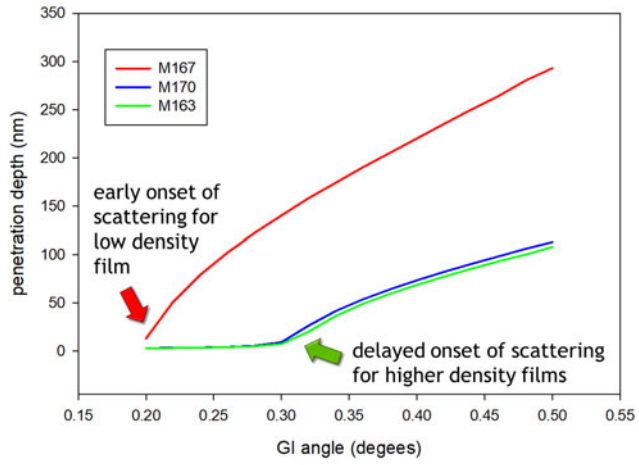

Figure 4. Modeling of penetration depth for films M163 (*c*-axis), M167 (*a*-axis), and M170 (amorphous) for Cu Kα radiation (8.05 keV). Note the delay in beam penetration until higher grazing incidence (GI) angles for both M163 and M170 films as compared to the low density M167 film.

will be severely limited until the beam sufficiently penetrates the film depth to provide signal to diffraction peak intensity. The use of delayed intensity onset in GIXRD patterns can serve for qualitatively determining high vs. low density films as shown here for M163 and M167, respectively. It could even potentially be expanded to become a quantifiable means of assessing density with proper modeling of the detection and growth of intensity as a function of grazing angle. The usefulness of this simple diagnostic cannot be overstated as this enables the isolation of the film density, a critical factor in determining desired film deposition characteristics. Coupled with this aspect of density determination is the straightforward qualitative assessment of crystallographic film orientation, which is easily verified from a simple viewing of the XRD patterns.

C. Thickness determination via GIXRF

One of the most common validation criteria for film acceptance is coating thickness. It is essential that a solid lubricant be sufficiently thick to endure the duty cycle required for the part as well as adequately coat all surfaces of a complex part with a minimum thickness due to shadowing. Therefore, having a means of determining thickness is essential for both tuning of a deposition process, and for quality control. XRF is well suited for film thickness by employing the Mo Kα emission line from the film, coupled with a reference signal from the substrate, e.g., the Fe Kα emission line. A simple ratio of these peak intensities can be employed to determine film thickness via proper modeling and calibration. This assumes that all other factors are equal, such as density and film composition. The Mo Kα emission line at ~17.4 keV serves as a good means of determining thickness since its X-ray energy will not suffer from attenuation as these X-rays traverse the thickness of the film on route back to the XRF detector. Hence, considerable depth can be probed for MoS_2 film thickness via the Mo Kα emission line. Note, however, the intensity of the Mo Kα signal yields no information regarding the S content in the film, and therefore will not enable diagnosis of actual film composition. XRF spectra *do* contain information concerning sulfur based on the S Kα and Kβ emission lines, but it is an unfortunate reality that these S peaks are overlapped by several of the Mo L emission lines, which obscure the sulfur emission lines (Thompson et al., 2009). Figure 5 shows a typical XRF spectrum obtained during our analysis illustrating the wealth of emission lines present. In this case, the spectra presented are for the M163 film. The main portion of the plot shows the appearance of the M163 XRF spectrum as measured at a grazing incidence angle of 2.0°. This grazing angle yields the highest depth of penetration for the grazing angle series and will therefore obtain the strongest signal from the substrate, as well as the highest Mo Kα

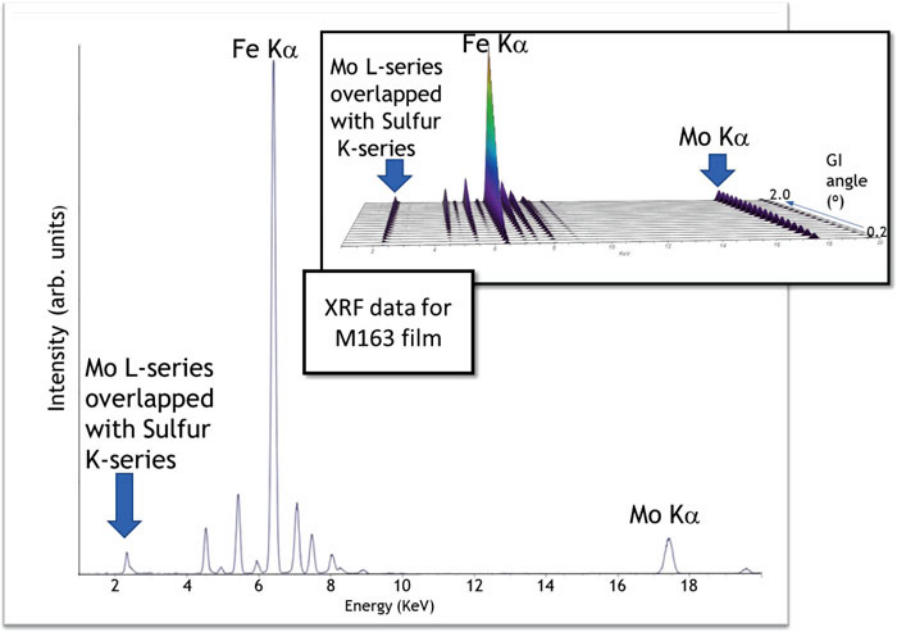

Figure 5. XRF spectrum for M163 film (grazing angle = 2.0°) as configured on the D500 GIXRD instrument. Note the presence of both the Mo Kα and Fe Kα peaks along with an overlapped profile at ~2.3 keV composed of overlapping Mo L-series and sulfur K-series emission lines. The inset plot shows the entire series of XRF spectra over the grazing angle series from 0.2° to 2.0°.

intensity from the film. There are many other peaks in the spectrum including emission lines from Ti, Cr, Fe, Ni, and Cu from the X-ray source. These elements are mostly from the substrate and are not included in our analysis, except for the Fe Kα peak which is employed as a reference intensity from the substrate. There is also an apparent doublet peak at ~2.3 keV. This apparent doublet is composed of both molybdenum L and sulfur K emission lines, as mentioned earlier. This low energy region of superimposed Mo and S peaks will be addressed in more detail later. The inset in Figure 5 shows spectra obtained from the entire grazing angle series. Note that while the Fe Kα peak intensity grows as a function of increased grazing angle, the Mo Kα intensity plateaus at the higher grazing angles, indicating that the full film is being penetrated. Therefore, to extract Fe Kα and Mo Kα peak intensities for thickness estimation, the peak profiles for Mo Kα and Fe Kα were evaluated from the GIXRF spectrum at 2.0° for all the films. Next, a Mo Kα/Fe Kα intensity ratio was calculated for each film and associated with the known film thickness of the sample per Table I. In this way, one would have confidence that the measured Mo signal was a summation over the entire film thickness, whether thick or thin.

Based on the extracted Mo Kα/Fe Kα ratios obtained for each film, a correlation of film thickness vs. the XRF emission line intensity ratio was derived. Figure 6 illustrates three separate plots, one for each method of film deposition. The *y*-axis of Figure 6 serves as ground truth (real) film thickness as determined by profilometer step height measurement of the film coatings. The *x*-axis shows the Mo Kα/Fe Kα integrated peak intensity ratio from XRF spectra at the grazing incidence angle of 2.0°. Each film series from Table I displays a different slope. The plot with the highest slope is from the *a*-axis film orientation which has the lowest density of the measured films, but also displays some of the highest S:Mo ratios. The lowest slope is from the amorphous film series. These amorphous films have high densities and the lowest S:Mo ratios, making them significantly sulfur-deficient. The plot having an intermediate slope is derived from the *c*-axis oriented films which have high densities and intermediate S:Mo ratios. It is clear from the plot that the composition of the film as well as the resulting density of the film will determine which graph should be used to estimate film thickness.

The challenge presented in Figure 6 is that there appears to be as many calibration curves for thickness as there are film deposition conditions presented in Table I. Knowledge of which calibration curve to employ for thickness estimation requires some additional knowledge of film stoichiometry and/or film density to make an appropriate determination. Incorrect assignment of the employed curve such as using the amorphous film calibration curve to determine the thickness of a low-density *a*-axis oriented film would grossly underestimate the film thickness. When considering the S:Mo composition values (listed on the plots in Figure 6 and derived from RBS measurements as reported in Table I), there is a connection between the slope of the line and the S:Mo ratio observed for the film. This composition dependence likely has ties to the density of the film which in turn is impacted by the grain growth, packing, and orientation (i.e., microstructure). Therefore, assessment of composition in terms of S:Mo ratio would serve well to direct assignment of the calibration curve employed for estimating the film thickness.

D. Film composition (S:Mo) via GIXRF

The low energy region of the XRF spectra contains the only means of extracting the sulfur signal as this is the location of the S Kα and Kβ peaks. Figure 7 shows a zoomed-in region for the GIXRF spectra of the M167 (*a*-axis oriented) and M170 (amorphous) films. These spectra were generated by averaging the final three spectra in the grazing angle series, notably the spectra collected at 1.8°, 1.9°, and 2.0°. This was done to improve the signal for the individual spectrum obtained for each film sample. Additionally, a 5-point smoothing method was applied to the final spectrum for each film to obtain improved profiles during fitting. Figure 7 illustrates a clear difference in appearance for the overall profile shape for the M167 and M170 films. The M170 spectrum shows a rise of a second peak in the ~2.4 keV range. This shoulder on the high energy side of the main peak in the spectrum is

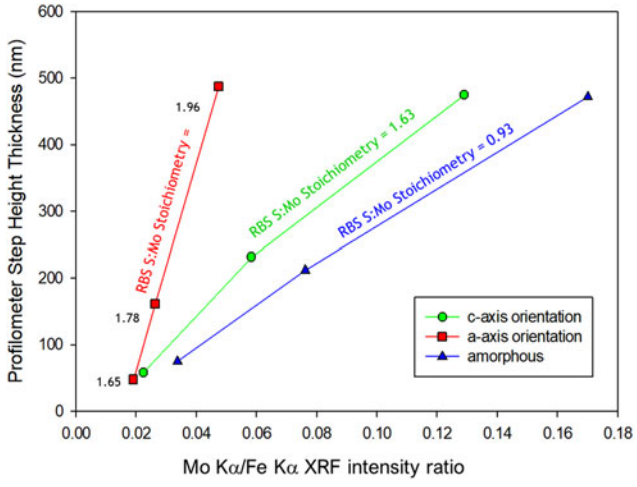

Figure 6. Film thickness as determined by profilometer step height measurement vs. the measured emission line intensity ratio of Mo Kα/Fe Kα intensity as determined from grazing angle = 2.0° spectra. RBS S:Mo ratios from Table I are also presented on the plot.

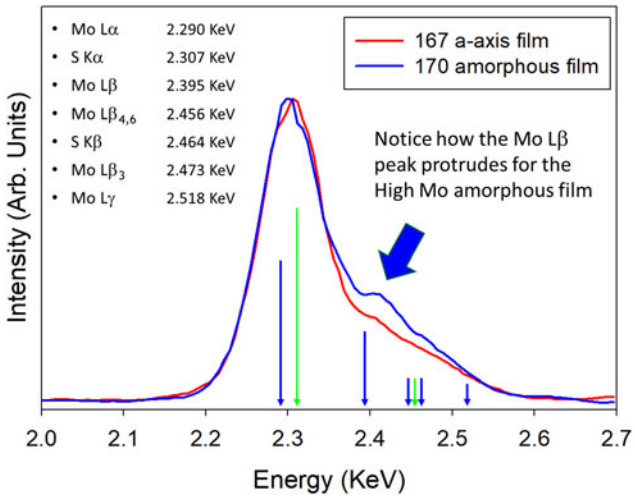

Figure 7. Zoomed-in low energy region of XRF spectra for film M167 and M170 illustrating the overlap of many of the Mo and S emission lines present to create the tail of intensity on the high energy side of the profile. Arrows indicate location of emission line energies for the Mo and S peaks. Reported emission line energies are taken from Thompson et al. (2009).

related mostly to the Mo Lβ peak. This peak is more pronounced in the M170 film as it is considerably sulfur-deficient (S:Mo ratio of 0.93), i.e., Mo-rich, compared to that of the M167 (S:Mo 1.96). It turns out that the peak overlap between the Mo L-series emission lines and that of the S K-series lines is considerably more complex. Figure 7 lists most of the possible XRF peaks that can occur for Mo and S over the defined range of 2.0 to 2.7 keV. The S lines are straightforward with only the S Kα (2.307 keV) and S Kβ (2.464 keV) emission lines present (Thompson et al., 2009). There are two peaks superimposed for the S Kα, the Kα_1 and Kα_2 peaks. The measurement resolution at this low energy region of the spectrum is insufficient to separate these very close energies; therefore, they are modeled as a single Kα emission line. The S Kα line resides very close to the Mo Lα emission line at 2.290 keV. Figure 7 shows the placement of these two peaks as illustrated by the blue and green arrows near the 2.3 keV location on the plot. These two major peaks in the profile account for most of the intensity and separating these profiles to obtain their respective integrated areas enables a quantitative assessment of the S and Mo content. The high energy tail to the right of these two overlapped peaks contains not only the presence of the Mo Lβ and S Kβ lines, but also comprises additional Mo L-series peaks including the Mo L$\beta_{4,6}$, the M Lβ_3 and the Mo Lγ emission lines. All of these peaks contribute to the tail present on the profile. In order to properly model the intensity, all of these peaks must be taken into account at some level. Since Mo L$\beta_{4,6}$, S Kβ, and Mo Lβ_3 all reside very close to one another in energy, and their intensity assignment is not essential for our modeling, these emission lines will be treated as a single peak termed S Kβ+ for the purposes of our profile modeling. The Mo Lβ and Mo Lγ peaks are relatively isolated in their energy locations and can each be treated as individual peak profiles. Therefore, the overall profile model would be composed of five peaks: Mo Lα, S Kα, Mo Lβ, S Kβ+, and Mo Lγ. Peak profile fitting was performed via the JadePro (Materials Data, Inc.) profile shape fitting routines. To obtain acceptable fitting outcomes, a number of constraints were required. First, all peak widths were constrained to the known instrument peak FWHM. This instrument width was determined by fitting of a weak Si Kα peak present at ~1.74 keV in each of the spectra. Second, a Pearson VII profile function was used to model the individual peak profiles, with the shape function coefficient constrained to be identical for all fitted peaks. Third, all peak locations were fixed at their known emission line positions. With these constraints in place, profile fitting converged well, but there were still some challenges.

It was noted in the initial refinement attempts that even small energy offsets in the spectra could significantly impact the outcome of the Mo Lβ and S Kα peaks since small deviations of the energy calibration on the *x*-axis can cause changes to the Mo Lα and S Kα integrated intensities. To improve this analysis, each spectrum was first corrected for minor energy errors by employing the Si Kα peak as a benchmark energy location because this peak was suitably isolated with a well-established emission line energy. This was not sufficient to optimize the modeling, as even a deviation of 5–10 eV could impact the refinement output in terms of resulting Mo Lα and S Kα intensity. Considering the relative isolation of the Mo Lβ peak as shown in Figure 7, an effort was made to employ this peak to serve as a guide to refinement optimization. The ratio of the Mo Lα to Mo Lβ intensity is established and constrained by the transition probabilities of the electron shells. This known ratio of intensity is 1 to ~0.47 for Mo Lα to Mo Lβ, respectively (Thompson et al., 2009). Therefore, a constraint was put in place to accept the resulting refinement if the Lβ to Lα ratio was between 0.45 and 0.50. This would give confidence that the fitting was modeling properly. An allowance was made for slight adjustments on keV axis of the spectrum to zero-in on the correct Mo Lβ to Lα intensity ratio. This final constraint enabled a good fitting protocol to model the overall profile and extract the Mo Lα and S Kα peak intensities.

Figure 8 illustrates the outcome of the fitting protocol for the M163 film. The resulting peak intensities reveal a slightly higher magnitude for the S Kα peak than that of the Mo Lα peak. The resulting ratio of the Mo Lβ to Mo Lα refined to 0.48, very close to the expected ratio of 0.47. The other peaks in the pattern labeled S Kβ+ and Mo Lγ round out the refinement and show a smooth fit of the overall profile, yielding a relatively flat difference curve. This analysis was performed for all the film samples to obtain the integrated peak areas of the Mo Lα and S Kα peaks. The ratio of these peaks was then compared to the S:Mo ratio as determined by RBS. It is worth noting, even though the Mo Lα and S Kα peaks proved challenging to separate without considerable constraints, compositional analysis is *enabled* because the X-ray penetration depth is essentially identical for Mo Lα and S Kα due to their very similar X-ray emission line energies and X-ray attenuation. Hence, the two emission lines will represent Mo and S content at essentially the same film depths for any and all grazing angle measurements.

Figure 9 shows a graph relating the S Kα/Mo Lα ratio as derived from the low energy region of GIXRF spectra to that of the ground truth (real) S:Mo ratio as determined by RBS. The relationship shows a clear trend in terms of composition. First, note the highly linear relationship between the S Kα/Mo Kα GIXRF ratio and the RBS S:Mo values. This confirms the ability to employ the GIXRF fitting model for predictive composition determination of the film samples. Second, note

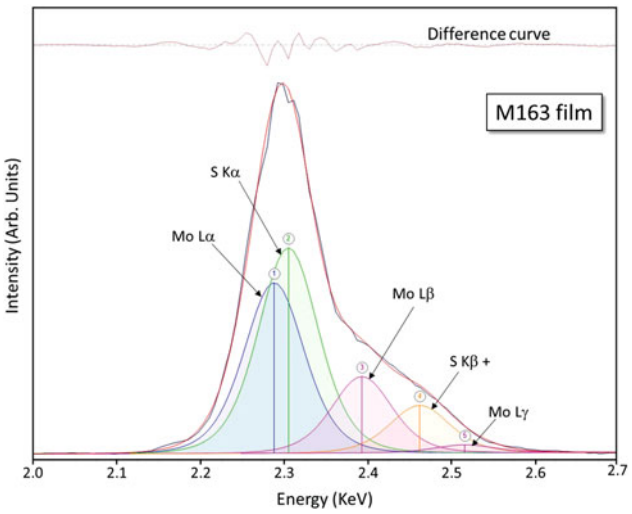

Figure 8. Resulting fit of emission lines for Mo L and S K-series peaks. This model, outlined in the text, establishes the ability to extract the intensity for the Mo Kα and S Kα peaks for means of quantifying film composition.

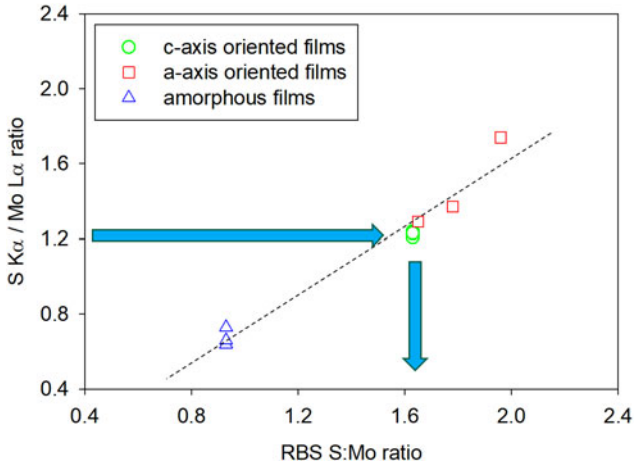

Figure 9. S Kα/Mo Lα intensity ratio as derived from the GIXRF vs. the ground truth (real) S:Mo ratio as determined by RBS. The nearly linear relationship confirms the ability to extract film chemistry from the low energy region of the GIXRF spectra obtained simultaneous to GIXRD measurements.

that the amorphous films (blue triangles) all cluster at the same values. This was also true for the *c*-axis oriented films (green circles). These results are understandable since all the amorphous films showed the same S:Mo RBS ratios and the same was true for the *c*-axis oriented film series. Hence, each series refined to similar S Kα/Mo Lα ratios from the GIXRF data, regardless of film thickness. The only film series that showed variation of the RBS S:Mo ratio was that of the *a*-axis films, which tended to show higher S:Mo ratios with increased film thickness (see Table I). This change in RBS S:Mo ratio was also detected in the GIXRF peak profile modeling, showing higher S Kα/Mo Lα intensity ratios for films that displayed higher RBS S:Mo ratios. Figure 9 demonstrates that with mindful attention to the modeling of these overlapped Mo and S peaks in the low energy region of the GIXRF spectra, a meaningful film composition in terms of S and Mo content can be derived. This is excellent news as it means that this final piece of the puzzle concerning the film characteristics can be extracted.

When considering the three different film deposition processes, it is worth highlighting that only the *a*-axis oriented films demonstrated variation in S:Mo composition with thickness. Specifically, the film series M167, M168, and M169 showed the highest S:Mo ratio of 1.96 for the thickest film (M167), but the thinnest film (M169) had a S:Mo ratio of 1.65, comparable to that of the *c*-axis oriented film having ~50 nm thickness, namely the M165 with S:Mo ratio of 1.63. This variation of S:Mo ratio for the *a*-axis film series is not fully understood. While we continue to investigate this phenomenon, we hypothesize that the growth rate increases as the coating gets thicker for these *a*-axis oriented films due to edge-oriented lamella that provide more reactive sites for incoming deposits to bond. These reactive sites allow for a higher percentage of ionized species, especially sulfur, to stick. Additionally, the lower ion energies of the RF deposition limit the effects of re-sputtering which preferentially occurs on light elements like sulfur.

Another important observation from the exemplar film series relates to the impact of sulfur deficiency on wear properties. We have observed that the S:Mo ratio correlates inversely to density. However, it is hard to decouple the effects of stoichiometry and density on wear behavior. That being said, it is our conjecture that changes in density outweigh that of stoichiometry. If the S:Mo ratio had a large influence, we would likely observe that high-density coatings which are sub-stoichiometric would display increased wear (M163 compared to M172), yet we see that wear is still improved. Under sliding conditions, even sub-stoichiometric coatings have been observed to recrystallize forming a few nanometer thick layer of basally oriented MoS_2. This shear-induced recrystallization provides a low friction interface and limits any impact of initial sub-stoichiometry to minor changes in early cycle friction.

The use of both GIXRD and GIXRF, collected simultaneously via the same instrumentation, can serve to extract the necessary information for determination of film quality. This method can enable qualification of a film deposition system as well as establish possible acceptance criteria for deposited films. A clear benefit of this methodology stems from the fact that both datasets can be obtained concurrently and in a nondestructive manner to speak to the functionality of the resulting film in terms of ultimate performance by identifying critical characteristics of the film including density, microstructure/texture, composition, and thickness. A limitation of this method is that the analysis requires the coating and substrate to be flat, whereas actual coated parts will likely have uneven surfaces.

IV. SUMMARY

Herein, we have described a means of nondestructive qualitative analysis of molybdenum disulfide coatings on steel substrates to access critical microstructural characteristics of the films deposited under varying process conditions. Film density can be assessed directly via GIXRD from the presence or absence of delayed onset of film scattering intensity as monitored via the grazing incidence angle series. This holds true for films showing amorphous nature as well as those showing crystalline peaks in the GIXRD series. Microstructure and crystalline orientation can easily be determined qualitatively from the GIXRD patterns collected. In addition, determination of the Mo and S content can be performed via the careful modeling of the low energy range of the GIXRF spectra to extract intensity from the Mo Lα and S Kα peaks. Finally, with the added benefit of composition and density assessment, thickness of the deposited films can more accurately be predicted via the use of established calibration curves. Taken together, the assessment of these four film characteristics will facilitate prediction of film performance and enable the establishing of acceptance criteria for films based on the use of this straightforward X-ray-based methodology.

ACKNOWLEDGMENTS

This work is supported by the Laboratory Directed Research and Development program at Sandia National Laboratories, a multimission laboratory managed and operated by National Technology and Engineering Solutions of Sandia, LLC., a wholly owned subsidiary of Honeywell International, Inc., for the U.S. Department of Energy's National Nuclear Security Administration under contract DE-NA-0003525. A

special thanks to Allyson Blanchard for her help with data reduction of the GIXRD patterns.

COMPETING INTERESTS

The authors declare none.

REFERENCES

Babuska, T., J. F. Curry, M. T. Dugger, P. Lu, Y. Xin, S. Klueter, A. C. Kozen, T. Grejtak, and B. A. Krick. 2022a. "Role of Environment on the Shear-Induced Structural Evolution of MoS_2 and Impact on Oxidation and Tribological Properties for Space Applications." *ACS Applied Materials & Interfaces* 14: 13914–24.

Babuska, T. F., J. F. Curry, M. T. Dugger, M. R. Jones, F. W. DelRio, P. Lu, Y. Xin, T. Grejtak, R. Chrostowski, F. Mangolini, N. C. Strandwitz, M. I. Chowdhury, G. L. Doll, and B. A. Krick. 2022b. "Quality Control Metrics to Assess MoS_2 Sputtered Films for Tribological Applications." *Tribology Letters* 70: 103.

Babuska, T. F., J. F. Curry, R. Thorpe, M. I. Chowdhury, N. C. Strandwitz, and B. A. Krick. 2023. "High-Sensitivity Low-Energy Ion Spectroscopy with Sub-Nanometer Depth Resolution Reveals Oxidation Resistance of MoS_2 Increases with Film Density and Shear-Induced Nanostructural Modifications of the Surface." *ACS Applied Nano Materials* 6: 1153–60.

Bassett, K. L., T. Watkins, J. Coleman, N. Bianco, L. S. Bailey, J. Pillars, S. G. Williams, T. F. Babuska, J. Curry, F. W. DelRio, A. A. Henriksen, A. Garland, J. Hall, B. A. Krick, and B. L. Boyce. 2023. "A Workflow for Accelerating Multimodal Data Collection for Electrodeposited Films." *Integrating Materials and Manufacturing Innovation* 12: 430–40.

Chason, E., and T. M. Mayer. 1997. "Thin Film and Surface Characterization by Specular X-Ray Reflectivity." *Critical Reviews in Solid State and Material Sciences* 22: 1–67.

Chrostowski, R., J. F. Curry, M. T. Dugger, N. Molina, T. F. Babuska, H. Celio, A. Dolocan, and F. Mangolini. 2023. "Spectroscopic Evaluation of Surface Chemical Processes Occurring in MoS_2 upon Aging." *ACS Applied Materials & Interfaces* 15: 37047–58.

Curry, J. F., N. Argibay, T. Babuska, B. Nation, A. Martini, N. C. Strandwitz, M. T. Dugger, and B. A. Krick. 2016. "Highly Oriented MoS_2 Coatings: Tribology and Environmental Stability." *Tribology Letters* 64: 11.

Curry, J. F., M. A. Wilson, H. S. Luftman, N. C. Strandwitz, N. Argibay, M. Chandross, M. A. Sidebottom, and B. A. Krick. 2017. "Impact of Microstructure on MoS_2 Oxidation and Friction." *ACS Applied Materials & Interfaces* 9: 28019–26.

Gao, X., M. Hu, J. Sun, Y. Fu, J. Yang, W. Liu, and L. Weng. 2017. "Response of RF-Sputtered MoS_2 Composite Films to LEO Space Environment." *Vacuum* 144: 72–79.

Henke, B. L., E. M. Gullikson, and J. C. Davis. 1993. "X-Ray Interactions: Photoabsorption, Scattering, Transmission, and Reflection at E = 50-30000 eV, Z = 1-92." *Atomic Data and Nuclear Data Tables* 54 (2): 181–342.

Hilton, M. R., and P. D. Fleischauer. 1992. "Applications of Solid Lubricant Films in Spacecraft." *Surface and Coatings Technology* 54/55: 435–41.

Khare, H. S., and D. L. Burris. 2014. "Surface and Subsurface Contributions of Oxidation and Moisture to Room Temperature Friction of Molybdenum Disulfide." *Tribology Letters* 53: 329–36.

Lince, J. R., S. H. Loewenthal, and C. S. Clark. 2019. "Tribological and Chemical Effects of Long Term Humid Air Exposure on Sputter-Deposited Nanocomposite MoS_2 Coatings." *Wear* 432-433: 202935.

Macknojia, A., A. Ayyagari, D. Zambrano, A. Rosenkranz, E. V. Shevchenko, and D. Berman. 2023. "Macroscale Superlubricity Induced by MXene/MoS_2 Nanocomposites on Rough Steel Surfaces under High Contact Stresses." *ACS Nano* 17: 2421–30.

Martens, G. 2023. Private Communication.

Thompson, A., I. Lindau, D. Attwood, Y. Liu, E. Gullikson, P. Pianetta, M. Howells, A. Robinson, K.-J. Kim, J. Scofield, J. Kirz, J. Underwood, J. Kortright, G. Williams, and H. Winick. 2009. *X-ray Data Booklet LBNL/PUB-490 Rev.3*. Berkeley, CA: Lawrence Berkeley National Laboratory. http://xdb.lbl.gov